Available online at www.sciencedirect.com
ScienceDirect
Journal of Computational Physics 224 (2007) 82–99
JOURNAL OF COMPUTATIONAL PHYSICS
www.elsevier.com/locate/jcp

The numerical simulation of liquid sloshing on board spacecraft

A.E.P. Veldman [a,*], J. Gerrits [a,1], R. Luppes [a], J.A. Helder [a], J.P.B. Vreeburg [b,2]

[a] Institute of Mathematics and Computing Science, University of Groningen, P.O. Box 800, 9700 AV Groningen, The Netherlands
[b] National Aerospace Laboratory NLR, P.O. Box 90502, 1006 BM Amsterdam, The Netherlands

Received 4 September 2006; received in revised form 10 December 2006; accepted 20 December 2006
Available online 10 January 2007

Abstract

The subject of study is the influence of sloshing liquid on the dynamics of spacecraft. A combined theoretical and experimental approach has been followed. On the one hand, CFD simulations have been carried out to predict the combined liquid/solid body motion. Basically a volume-of-fluid (VOF) approach is followed, however with improvements in the treatment of the free liquid surface: these cover the surface reconstruction and displacement and the calculation of surface tension effects by means of a local height function. Also attention has been paid to the stability of the numerical coupling between solid-body dynamics and liquid dynamics. On the other hand, in-orbit experiments have been carried out with the Sloshsat FLEVO satellite. The paper describes a first comparison between theoretical predictions and experimental findings.

PACS: 47.11.−j; 47.55.N−; 45.20.D−

Keywords: Free-surface flow; Sloshing; Microgravity; Spacecraft dynamics; Sloshsat FLEVO; Solid–liquid interaction; Computational fluid dynamics

1. Introduction

With the increasing amount of liquid on board spacecraft, liquid management and its influence on the overall spacecraft dynamics is becoming increasingly important. The influence of sloshing liquid may hamper critical manoeuvres in space, such as the docking of liquid-cargo vehicles or the pointing of observational satellites. Several serious problems with sloshing liquid in spacecraft have been reported over the years. For example, during the last seconds of the first lunar landing in 1969, sloshing of the remaining propellant induced an oscillatory motion of the Apollo 11 Lunar Module (well visible in the video footage), which hampered accurate control of the landing manoeuvre [1]. Another example is the NEAR (Near Earth Asteroid

* Corresponding author. Tel.: +31 50 3633988; fax: +31 50 3633800.
E-mail addresses: veldman@math.rug.nl (A.E.P. Veldman), jeroen.gerrits@vortech.nl (J. Gerrits), jan.vreeburg@gmail.com (J.P.B. Vreeburg).
[1] Present address: VORtech B.V., P.O. Box 260, 2600 AG Delft, The Netherlands.
[2] Present address: Gerbrandylaan 23, 2314 EX Leiden, The Netherlands.

0021-9991/$ - see front matter
doi:10.1016/j.jcp.2006.12.020

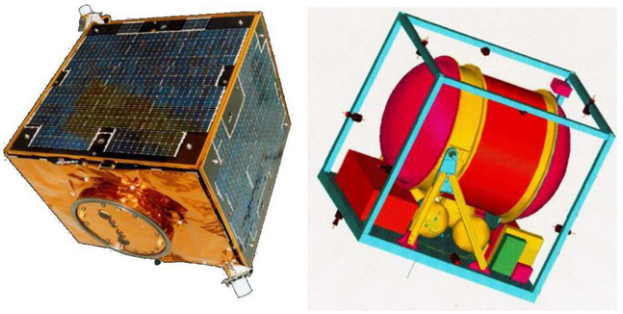

Fig. 1. Left: The Sloshsat FLEVO satellite. Right: A mock-up view inside Sloshsat.

Rendezvous) mission to the asteroid Eros in 1998. During an orbital correction the spacecraft experienced unexpected motion and went into safety mode. Fortunately, the mission could be recovered, although at the cost of a 13-month delay. Fuel slosh was identified as the probable cause [2].

The study of the combined liquid–solid body dynamics is being carried out with both theoretical and experimental means. The theoretical study makes use of computational fluid dynamics (CFD) techniques for free-surface flow; experiments have been carried out with the Sloshsat FLEVO[3] mini satellite (Fig. 1), designed and built by the Dutch National Aerospace Laboratory NLR [3]. An overview of the relevant physics and modelling techniques for sloshing liquids in space is given by Vreeburg and Veldman [4]. Specific scientific areas in liquid dynamics where knowledge is lacking are contact-line behaviour and damping. The Sloshsat experiments have been designed to give more information on these issues [5].

During the spacecraft motion, the liquid configuration can vary easily, in shape as well as in topology. This is in contrast with terrestrial applications where gravity tends to keep the liquid down. To simulate such dynamically changing liquid configurations, a large amount of flexibility has to be present in the numerical approach. It is no longer sufficient to apply a boundary-element philosophy [6,7]. A field method is used instead, mostly based on the Navier–Stokes equations, including a 'bookkeeping' system for tracking the position of the liquid and its free surface [8]. Several approaches can be found in the literature, of which a short assessment will be given next.

The Marker-and-Cell (MAC) method is the 'father' of all free-surface flow methods [9], and makes use of massless particles to keep track of the liquid region. Accuracy requires a considerable number of particles per grid cell, making the method computationally expensive, especially in 3D. A cheaper way is to apply only surface markers [10], but now splitting and merging of the surface are difficult to handle. The MAC follow-up is the volume-of-fluid (VOF) method introduced by Hirt and Nichols [11]. Here a discrete indicator (or color) function is used that corresponds to the cell volume occupied by fluid. The original version of the reconstruction and displacement algorithm leads to considerable 'flotsam and jetsam', i.e. artificial drops that numerically pinch off [12,13]. Due to rounding errors, also limited loss or gain of mass is observed, although in principle VOF is mass conserving since it is a finite-volume method. Variants of VOF can be designed that can track an arbitrarily moving free surface with high reliability [12,14]. Mass conservation can be ensured exactly by using a local height function [15,16]; this approach bears some resemblance with the segment projection method used in a Lagrangian setting [17,18]. A VOF variant that suffers less from mass loss is the piecewise linear reconstruction method (PLIC) introduced by Youngs [19]. Another successful member of this family is Yabe's CIP method [20].

An alternative to the indicator-function methods is the level set method [21,22], which makes use of a function representing the distance to the liquid surface. Reconstruction of the free surface is conceptually simpler than with the VOF method. However, for violently moving free surfaces the level set function requires to be redefined regularly, and conservation of the amount of liquid is a serious issue [23–25]. To reduce mass loss, the level set method is sometimes combined with the VOF method [26,27].

[3] The acronym FLEVO stands for Facility for Liquid Experimentation and Verification in Orbit; it also refers to the Dutch province (Flevoland) where the NLR Space Division is located. Sloshsat FLEVO was launched February 12, 2005.

In moving-grid methods, also known as ALE (Arbitrary Lagrangian Eulerian) methods [28], at each time step the grid is fitted to the moving free surface in a Lagrangian manner. In this way it is easier to apply boundary conditions, but when the free surface undergoes large deformation these methods are less suitable. The largest flexibility is offered by gridless methods like smoothed particle hydrodynamics (SPH) [29]. Their application to fluid dynamics is very young; thus far only limited comparisons with other methods have been made [30].

In the absence of gravity, and at low velocity, capillary effects at the free liquid surface, such as surface tension and wetting characteristics, are dominating liquid motion. Therefore, special attention has to be paid to the modelling and implementation of surface curvature effects and contact-line behaviour. The inclusion of curvature effects can give rise to the so-called spurious (or parasitic) velocities. Accurate calculation of the curvature can reduce the effect [31–35]; using the earlier-mentioned local height function turns out to be profitable. The curvature effect can be implemented as an explicit boundary condition for the pressure at the free surface [9], or as a body force in the Navier–Stokes equations like the CSF method [36]. Both approaches appear similarly susceptible to parasitic currents [34].

The presented simulation method COMFLO is a further development of the SAVOF method used in the early 1980s as a support to experiments on board Spacelab [37]. Its first validation for microgravity fluid dynamics was in the analysis of the Wet Satellite Model experiment, which flew on a sounding rocket in 1992 [38,39]. Currently, COMFLO is also used for maritime, industrial and offshore free-surface flow applications [16,40,41] and in biomedical applications [42–44]. Sections 2 and 3 describe its mathematical and numerical contents; the validation with the Sloshsat FLEVO experiments is presented in Section 4.

2. The mathematical model

2.1. Liquid dynamics

The Sloshsat tank is partially filled with distilled water. The flow inside the tank is described with a one-phase model, i.e. liquid plus void; the liquid is considered incompressible and isothermal. In reality, the void region is filled with air (at atmospheric pressure). But in view of the low density and the low viscosity of the air, its influence on the liquid motion is neglected.

The fluid motion is described by means of conservation of mass

$$\nabla \cdot \boldsymbol{u} = 0 \tag{1}$$

and conservation of momentum, which in a moving tank-fixed reference frame is given by

$$\frac{\partial \boldsymbol{u}}{\partial t} + (\boldsymbol{u} \cdot \nabla)\boldsymbol{u} = -\frac{1}{\rho}\nabla p + \frac{\mu}{\rho}\Delta \boldsymbol{u} + \boldsymbol{f}. \tag{2}$$

Here $\boldsymbol{u}$ denotes the velocity of the fluid relative to the tank, p the pressure, and ρ and μ the fluid density and viscosity, respectively. The vector $\boldsymbol{f}$ represents a virtual body force induced by the motion of the tank (see Section 2.3). These equations are only applied in the liquid region.

A schematic overview of the required boundary conditions is given in Fig. 2. The usual no-slip boundary condition for viscous flow is applied at the tank wall, i.e. $\boldsymbol{u} = 0$. Stress balance at the free surface in normal ($\boldsymbol{n}$) and tangential ($\boldsymbol{t}$) direction gives

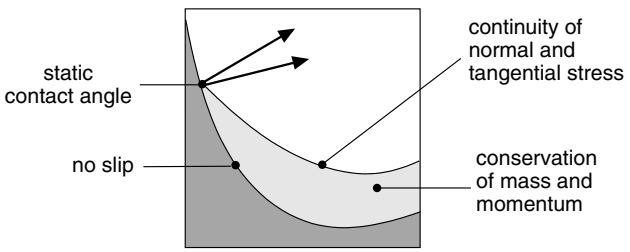

Fig. 2. Schematic overview of the liquid model. Dark and light shading represent solid body and liquid, respectively.

$$-p + 2\mu\frac{\partial u_n}{\partial \boldsymbol{n}} = -p_0 + 2\sigma\kappa, \quad \mu\left(\frac{\partial u_n}{\partial \boldsymbol{t}} + \frac{\partial u_t}{\partial \boldsymbol{n}}\right) = 0. \tag{3}$$

The former condition is often simplified to $p = p_0 - 2\sigma\kappa$ when the viscous term is relatively small. In these equations u_n and u_t denote the normal and tangential velocity at the free surface, respectively. Furthermore, p_0 denotes the ambient pressure of the air in the tank, σ the surface tension of the fluid and κ the mean curvature of the free surface.

The contact angle θ between the free liquid surface and the solid wall depends on the material properties of liquid (water), air and the tank wall (polyethylene); it is taken $\theta = 90°$ in this study. However, in case the contact line sticks to the tank wall the contact angle may not be constant. Thus, as an alternative, a dynamic contact angle in combination with contact-angle hysteresis might be useful. Recent validation of such a method, using free-fall drop tower experiments, shows promising results. For more details and references, see Van Mourik et al. [45].

In the absence of effective gravity (i.e. vanishing Bond number), surface tension forces mainly 'compete' with inertial forces. Their balance is indicated by the Weber number $We \equiv \rho L U^2/\sigma$, where L and U are a characteristic length and velocity scale of the Sloshsat FLEVO tank, respectively. The experiments have been designed such that $We = O(1 - 40)$, i.e. capillary effects are highly relevant. Therefore, accurate calculation of the curvature featuring in (3) is important; we return to this issue in Section 3.2.3.

2.2. Solid-body dynamics

Attached to Sloshsat is a (moving) coordinate system; its origin does not have to coincide with the spacecraft center of mass (which is fluctuating in time due to the liquid motion). Let $\boldsymbol{\omega}$ and $\dot{\boldsymbol{\omega}}$ denote the angular velocity and acceleration of the moving frame, respectively, whereas $\dot{\boldsymbol{q}}$ is the linear acceleration of the origin of the moving reference frame relative to the inertial frame. In terms of these quantities, the governing equations for the solid-body dynamics, describing conservation of linear and angular momentum, are given by

$$m_s\dot{\boldsymbol{q}} + \dot{\boldsymbol{\omega}} \times m_s\bar{\boldsymbol{r}}_s + \boldsymbol{\omega} \times (\boldsymbol{\omega} \times m_s\bar{\boldsymbol{r}}_s) = \mathscr{F} + \boldsymbol{F}_{thr}, \tag{4}$$

$$m_s\bar{\boldsymbol{r}}_s \times \dot{\boldsymbol{q}} + \boldsymbol{I}_s\dot{\boldsymbol{\omega}} + \boldsymbol{\omega} \times \boldsymbol{I}_s\boldsymbol{\omega} = \mathscr{T} + \boldsymbol{T}_{thr}. \tag{5}$$

Here, m_s, $\bar{\boldsymbol{r}}_s$ and $\boldsymbol{I}_s$ denote the mass, center of mass and moment-of-inertia (MOI) tensor of the 'dry' Sloshsat, respectively (the latter two quantities are taken relative to the origin of the moving reference frame). The vectors $\mathscr{F}$ and $\mathscr{T}$ represent the force and corresponding torque that the fluid exerts on the wall of the Sloshsat tank via pressure (normal stress) and viscous effects (tangential stress). Note that these quantities are roughly proportional to the liquid mass, which has relevant algorithmic implications as we will see below. Finally, $\boldsymbol{F}_{thr}$ gathers the thruster-induced forces on the spacecraft; their induced torque $\boldsymbol{T}_{thr} = \boldsymbol{r}_{thr} \times \boldsymbol{F}_{thr}$ is short-hand notation for a summation over all individual thrusters at locations symbolized by $\boldsymbol{r}_{thr}$ (in the moving frame).

2.3. Coupled liquid–solid body dynamics

The description of the interaction between the sloshing fluid inside the Sloshsat tank and the motion of the spacecraft itself requires a coupling between the two models for fluid dynamics (Section 2.1) and solid-body dynamics (Section 2.2).

The influence of the solid-body motion on the fluid is described in the moving coordinate system through the virtual body force

$$\boldsymbol{f} = -\dot{\boldsymbol{q}} - \dot{\boldsymbol{\omega}} \times \boldsymbol{r} - \boldsymbol{\omega} \times (\boldsymbol{\omega} \times \boldsymbol{r}) - 2\boldsymbol{\omega} \times \boldsymbol{u}, \tag{6}$$

which is used in Eq. (2). Conversely, the influence of the sloshing liquid on the solid body in (4) + (5) is in first instance described by

$$\mathscr{F} = \oint_{\partial V} (p\boldsymbol{I}_3 - \mu\nabla\boldsymbol{u}) \cdot \boldsymbol{n}\,\mathrm{d}S, \tag{7}$$

$$\mathscr{T} = \oint_{\partial V} (\boldsymbol{r} \times (p\boldsymbol{I}_3 - \mu\nabla\boldsymbol{u})) \cdot \boldsymbol{n}\,\mathrm{d}S. \tag{8}$$

Here $\boldsymbol{I}_3$ is the 3×3 identity matrix and $\boldsymbol{n}$ the outward-pointing normal on the boundary ∂V of the total volume V of the Sloshsat tank. Using the divergence theorem, these integrals can be written as integrals over the total volume V

$$\mathscr{F} = \int_V \nabla p - (\nabla \cdot \mu \nabla)\boldsymbol{u}\,\mathrm{d}V = -\int_V \rho\left(\frac{\mathrm{D}\boldsymbol{u}}{\mathrm{D}t} - \boldsymbol{f}\right)\mathrm{d}V,$$

$$\mathscr{T} = \int_V \boldsymbol{r} \times (\nabla p - (\nabla \cdot \mu \nabla)\boldsymbol{u})\,\mathrm{d}V = -\int_V \rho \boldsymbol{r} \times \left(\frac{\mathrm{D}\boldsymbol{u}}{\mathrm{D}t} - \boldsymbol{f}\right)\mathrm{d}V,$$

where the Navier–Stokes equations (1)+(2) are used to deduce the expressions in terms of the material derivative $\mathrm{D}\boldsymbol{u}/\mathrm{D}t$. The integration is over the full volume V of the tank, i.e. both the liquid volume and the void. Hereto, the density in the void is set to zero.

In the equations for the solid-body dynamics (4) + (5), the left-hand sides contain the mass of the solid body, while the right-hand side is proportional to the mass of the liquid. Intuitively, one can feel that solving the system in a hierarchical way, may lead to an unstable procedure when the liquid mass is too large compared to that of the solid body. Therefore, the system for the coupled solid-body dynamics is rewritten: all contributions from $\boldsymbol{f}$ that are independent of $\boldsymbol{u}$, see (6), are moved to the left-hand sides of (4) and (5), where they can be combined with similar terms for the solid body. The final equations for the coupled solid-body dynamics thus read

$$m\dot{\boldsymbol{q}} + \dot{\boldsymbol{\omega}} \times m\bar{\boldsymbol{r}} + \boldsymbol{\omega} \times (\boldsymbol{\omega} \times m\bar{\boldsymbol{r}}) = -\int_V \rho\left(\frac{\mathrm{D}\boldsymbol{u}}{\mathrm{D}t} + 2\boldsymbol{\omega} \times \boldsymbol{u}\right)\mathrm{d}V + \boldsymbol{F}_{\mathrm{thr}}, \tag{9}$$

$$m\bar{\boldsymbol{r}} \times \dot{\boldsymbol{q}} + \boldsymbol{I}\dot{\boldsymbol{\omega}} + \boldsymbol{\omega} \times \boldsymbol{I}\boldsymbol{\omega} = -\int_V \rho \boldsymbol{r} \times \left(\frac{\mathrm{D}\boldsymbol{u}}{\mathrm{D}t} + 2\boldsymbol{\omega} \times \boldsymbol{u}\right)\mathrm{d}V + \boldsymbol{T}_{\mathrm{thr}}. \tag{10}$$

In these equations, $m = m_{\mathrm{s}} + m_{\mathrm{l}}$ is the total mass (solid + liquid) of Sloshsat, $\boldsymbol{I} = \boldsymbol{I}_{\mathrm{s}} + \boldsymbol{I}_{\mathrm{l}}$ is the moment-of-inertia tensor of the total system, whereas $\bar{\boldsymbol{r}} = (m_{\mathrm{s}}\bar{\boldsymbol{r}}_{\mathrm{s}} + m_{\mathrm{l}}\bar{\boldsymbol{r}}_{\mathrm{l}})/m$ is the center of mass of the coupled system. Since the mass of the liquid (which appears on the right-hand side of the equations) will always be smaller than the total mass of the coupled system (on the left-hand side), a hierarchical liquid–solid coupling algorithm within the system (9) + (10) will not interfere with the stability of time integration (see Section 3.4).

3. The numerical model

3.1. Cartesian cut-cell method

To solve the Navier–Stokes equations numerically, the computational domain is covered with a fixed Cartesian grid. This makes grid generation easier; moreover much research has been done on numerical tracking of free surfaces on Cartesian grids, e.g. [12,14]. A disadvantage of a rectangular grid is that the curved solid boundary of the water tank inside Sloshsat is not aligned with the computational cell faces. To avoid staircase geometries, the geometry is chosen piecewise linear, cutting through the computational cells: in this way a so-called cut-cell method is created [46,47]. Our cut-cell approach, summarized below, has especially been designed for accurate simulation of turbulent flow, where the challenge is in resolving the thin boundary layers along the curved walls. First experiences with the method can be found in [47].

3.1.1. Apertures

In order to describe the flow domain, in every grid cell a volume aperture F^{b} and face apertures A^x, A^y and A^z are introduced, indicating the fraction of a cell or cell face that is open for flow. Apart from these geometry apertures, also a free-surface aperture F^{s} is introduced, indicating the fraction of a cell that is actually filled with fluid. This aperture is also known as the volume-of-fluid (VOF) function introduced by Hirt and Nichols [11]. In Fig. 3, using 'compass' notation, a two-dimensional illustration of these apertures is given, where δx and δy denote the mesh size in x- and y-direction, respectively. The volume apertures for the geometry and free-surface are related by $0 \leqslant F^{\mathrm{s}} \leqslant F^{\mathrm{b}} \leqslant 1$.

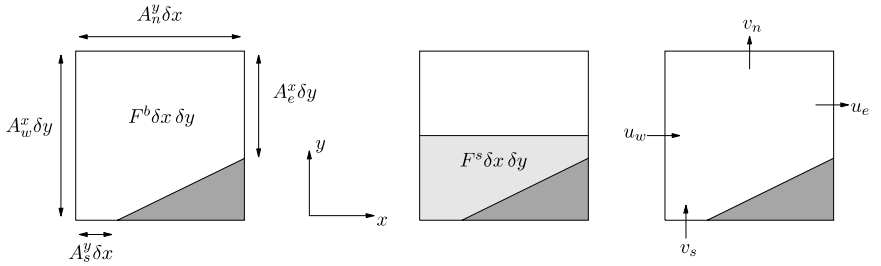

Fig. 3. Two dimensional illustration of the volume and edge apertures for the geometry (left), the volume aperture for the free surface (middle) and the positioning of the velocities (right). Dark and light shading represent solid body and liquid, respectively.

The geometry apertures are calculated in a pre-processing phase. The shape of the object is given as a CAD/CAM description in terms of elementary building blocks: bricks, cylinders, spheres, etc. Each face and each cell of the computational grid is virtually covered by a large number of points. For each of these points it is decided whether it is lying inside or outside the object. The fraction determines the face and volume apertures, respectively.

For the spatial discretization a finite-volume method is applied, hence Eqs. (1) and (2) are rewritten in integral conservation form. The computational domain is divided in control volumes, with the flow variables staggered as in the original MAC method [9]. The velocity components (u, v, w) are defined at cell faces, in the center of the part of the face that is open to flow (Fig. 3 (right)); the pressure p is defined in open cell centers.

The continuity equation (1) is discretized with the computational cell shown in Fig. 3, making use of the apertures. The discrete sum of all mass fluxes through the boundary ∂V of the computational cell should vanish. For the two-dimensional computational cell in Fig. 3 this results in

$$u_e A_e^x \delta y + v_n A_n^y \delta x - u_w A_w^x \delta y - v_s A_s^y \delta x = 0. \tag{11}$$

3.1.2. Conservation of momentum

The spatial discretization of the convection, diffusion and pressure terms in Eq. (2) is obtained in a similar way at all faces between cells that contain fluid. For uncut cells as well as cut cells, the momentum control volumes are defined as half of the open parts of both neighbouring cells; Fig. 4 shows a control volume for x-momentum (dashed demarcated region).

The volume integral of the time derivative in Eq. (2) is discretized in space using the midpoint rule with volume $\frac{1}{2}(F_e^b \delta x_e + F_w^b \delta x_w)\delta y$, where F_e^b and F_w^b are the volume apertures of the eastern and western cell, respectively.

The convective fluxes are found by multiplying the mass fluxes m_r, m_d, m_l and m_u through the right, lower, left and upper boundaries, respectively, with the scalar horizontal velocity u at the respective boundaries. The discretization becomes

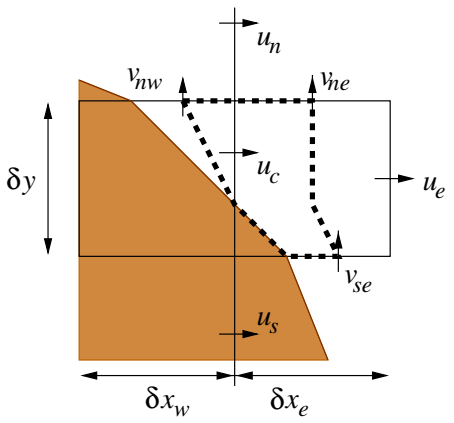

Fig. 4. The discretization of convective terms near the boundary (shaded area). The control volume is demarcated by the dashed line.

$$\oint_{\partial V} u\boldsymbol{u}\cdot\boldsymbol{n}\,\mathrm{d}S \doteq m_\mathrm{r}u_\mathrm{r} - m_\mathrm{d}u_\mathrm{d} - m_\mathrm{l}u_\mathrm{l} + m_\mathrm{u}u_\mathrm{u} = \frac{1}{2}(m_\mathrm{r}u_\mathrm{e} - m_\mathrm{d}u_\mathrm{s} - m_\mathrm{l}u_\mathrm{w} + m_\mathrm{u}u_\mathrm{n}) + \frac{1}{2}(m_\mathrm{r} - m_\mathrm{d} - m_\mathrm{l} + m_\mathrm{u})u_\mathrm{c}, \tag{12}$$

with the mass fluxes given by

$$m_\mathrm{r} = \frac{1}{2}(u_\mathrm{e}A^x_\mathrm{e}\delta y + u_\mathrm{c}A^x_\mathrm{c}\delta y) \quad \text{and} \quad m_\mathrm{d} = \frac{1}{2}(v_\mathrm{se}A^y_\mathrm{se}\delta x_\mathrm{e} + v_\mathrm{sw}A^y_\mathrm{sw}\delta x_\mathrm{w}). \tag{13}$$

Similar expressions hold for m_l and m_u. Applying Eq. (11) in the adjacent cells shows that the coefficient of the central velocity u_c in Eq. (12) vanishes. This makes the convective contribution to the coefficient matrix skew symmetric, like the continuous operator, which is a favourable property [48]. Also, it can be proven that with this discretization small cut cells do not influence the usual stability limits of time integration [47]. Artificial diffusion and dispersion are added to transfer the central discretization of the convective term into a (more stable) symmetry-preserving second-order upwind discretization [49].

The pressure gradient in the x-momentum equation is discretized as a boundary integral

$$\oint_{\partial V} pn_x\,\mathrm{d}S \doteq (p_\mathrm{e} - p_\mathrm{w})A^x_\mathrm{c}\delta y. \tag{14}$$

Here, p_e and p_w are the pressure in the eastern and western cells, respectively (Fig. 4), and A^x_c is the edge aperture of the cell face where the central velocity is defined. Thus the discrete gradient is the negative transpose of the discrete divergence operator Eq. (11), similar to their analytic relation $\nabla = -(\nabla\cdot)^\mathrm{T}$ [48]. An external force like gravity, not present in the current application, would be written as $F_\mathrm{g} = -\nabla gz$, to be discretized similar to the pressure gradient. In this way, it can exactly cancel the discrete hydrodynamic pressure.

3.1.3. Time integration

For the temporal derivatives in Eq. (2) the Adams-Bashforth method is used. The combination of temporal and spatial discretization leads to

$$\mathscr{M}\boldsymbol{u}_h^{n+1} = 0, \tag{15}$$

$$\mathscr{V}\frac{\boldsymbol{u}_h^{n+1} - \boldsymbol{u}_h^n}{\delta t} + \mathscr{C}(\boldsymbol{u}_h^*)\boldsymbol{u}_h^* = -\frac{1}{\rho}\mathscr{P}\boldsymbol{p}_h^{n+1} + \frac{\mu}{\rho}\mathscr{D}\boldsymbol{u}_h^* + \boldsymbol{f}_h^*, \tag{16}$$

with $(\cdot)^* = \frac{3}{2}(\cdot)^n - \frac{1}{2}(\cdot)^{n-1}$. Here $\boldsymbol{u}_h$, $\boldsymbol{p}_h$ and $\boldsymbol{f}_h$ are vectors containing all discrete velocities, pressures and forces, respectively, and $\mathscr{M}$, $\mathscr{V}$, $\mathscr{P}$, $\mathscr{C}$ and $\mathscr{D}$ denote coefficient matrices. The matrix $\mathscr{V}$ is a diagonal matrix containing cell volumes. The matrices $\mathscr{M}$ and $\mathscr{P}$ are related through $\mathscr{P} = -\mathscr{M}^\mathrm{T}$, reflecting that analytically the divergence operator and the gradient operator are adjoint. The matrices $\mathscr{C}$ and $\mathscr{D}$ correspond to the discretized convective and diffusive (including the artificial diffusion) operators; they are skew-symmetric and symmetric, respectively, like their continuous counterparts [48].

Combination of Eqs. (15) and (16) leads to the Poisson equation for the pressure $\boldsymbol{p}_h^{n+1}$

$$-\mathscr{M}\mathscr{V}^{-1}\mathscr{M}^\mathrm{T}\boldsymbol{p}_h^{n+1} = \frac{\rho}{\delta t}\mathscr{M}\tilde{\boldsymbol{u}}_h, \tag{17}$$

in which the auxiliary velocity field $\tilde{\boldsymbol{u}}_h$ is defined as

$$\tilde{\boldsymbol{u}}_h = \boldsymbol{u}_h^n + \delta t\mathscr{V}^{-1}\left(-\mathscr{C}(\boldsymbol{u}_h^*)\boldsymbol{u}_h^* + \frac{\mu}{\rho}\mathscr{D}\boldsymbol{u}_h^* + \boldsymbol{f}_h^*\right).$$

At the free surface, the boundary condition (3) for the pressure is included as described in Section 3.2.3. Because of this free-surface condition, the Poisson matrix in (17) becomes non-symmetric and even may loose diagonal dominance. To handle this, Eq. (17) is solved iteratively using a SOR method with automatically adjusted relaxation parameter for optimal convergence behaviour that is fully robust [50]. Due to the good initial guess from the previous time step, this method is highly competitive in comparison with preconditioned Krylov subspace methods; also it is highly parallelizable and vectorizable. Once the pressure $\boldsymbol{p}_h^{n+1}$ at the new time level is determined, it is subsequently substituted in Eq. (16) to obtain the new velocity field $\boldsymbol{u}_h^{n+1}$. For more details, see [15,16,40,41].

3.2. The free liquid surface

The presence of a free liquid surface requires some kind of 'bookkeeping' system to identify the position of the liquid. Here, the original MAC labeling system is used [9]. The reconstruction of the free surface is done with either classical VOF (SLIC) [11] or PLIC [19], however combined with a local height function to avoid over- and underflow of the VOF function during surface displacement. The height function is also used to determine the surface curvature. We will next discuss these aspects in some detail.

3.2.1. Free-surface reconstruction

Making use of the apertures F^{b} for the solid body and F^{s} for the liquid (see Section 3.1.1), every grid cell can be given a label. A distinction is made between five different types of computational cells. The interior cells containing no fluid, i.e. $F^{\mathrm{b}} > 0$ and $F^{\mathrm{s}} = 0$, are labeled as E(mpty) cells. Non-empty cells ($F^{\mathrm{s}} > 0$) adjacent to E cells are labeled as S(urface) cells, as they must contain part of the free surface. All the remaining non-empty cells are labeled F(luid) cells. Cells satisfying $F^{\mathrm{s}} = F^{\mathrm{b}} = 0$ are called B(oundary) cells when they are adjacent to an interior cell, otherwise they are labeled as (e)X(terior). In Fig. 5 an example of a label configuration is shown.

For every surface cell, locally a function is defined that gives the height of the fluid in a column or row of three cells. The direction in which the function is defined is aligned with the coordinate axis that (in computational space) is 'most normal' to the free surface, where the direction of the cell diagonal acts as the 'neutral' position [51] (Fig. 6). The approach is equivalent with a local transformation to a unit cell and applying a 'largest-component-of-the-normal' criterion as in e.g. [34]. Thus, the components of the normal $\boldsymbol{n} \propto \nabla F^{\mathrm{s}}$ are first approximated by a central discretization: with reference to Fig. 6 in two dimensions $\boldsymbol{n} \propto ((F^{\mathrm{s}}_{\mathrm{e}} - F^{\mathrm{s}}_{\mathrm{w}})/(2\delta x), (F^{\mathrm{s}}_{n} - F^{\mathrm{s}}_{\mathrm{s}})/(2\delta y))^{\mathrm{T}}$. To account for the diagonal direction, these components are multiplied by their corresponding grid size, and finally the maximum component is sought. Hence the surface orientation is determined by (in 2D) $\max\{|F^{\mathrm{s}}_{\mathrm{e}} - F^{\mathrm{s}}_{\mathrm{w}}|, |F^{\mathrm{s}}_{\mathrm{n}} - F^{\mathrm{s}}_{\mathrm{s}}|\}$. In this way, the criterion also applies for highly elongated computational cells as shown in Fig. 6. When the solid wall intersects the cells involved, i.e. $F^{\mathrm{b}} < 1$, F^{s} has to be replaced by $F^{\mathrm{s}} + (1 - F^{\mathrm{b}})$.

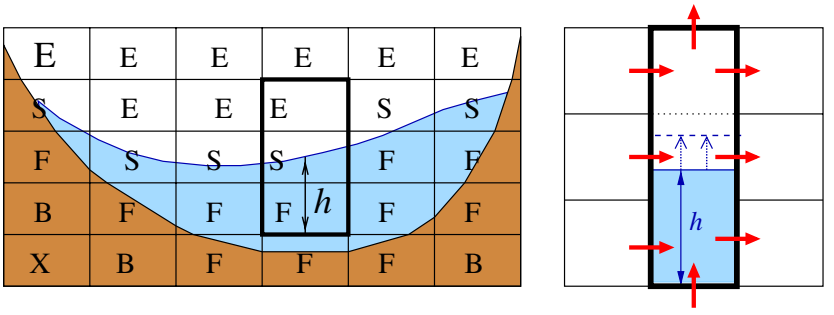

Fig. 5. Left: Two dimensional grid-cell labeling and definition of the height function h for a surface cell S. Dark and light shading represent solid body and liquid, respectively. Right: Update of height function.

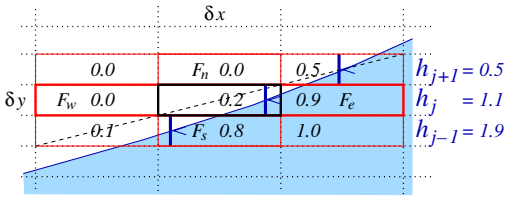

Fig. 6. The slope of the cell diagonal (dashed) decides between horizontal and vertical: the figure shows a 'vertical' free surface.

3.2.2. Free-surface displacement

When the new velocity field at time level $n+1$ is known, the free surface can be displaced. Basically, the evolution of the free surface satisfies

$$\frac{\partial F^s}{\partial t} + (\boldsymbol{u}\cdot\nabla)F^s = 0. \tag{18}$$

This equation is solved using an adapted version of the VOF method [11]. In principle, mass fluxes across cell faces are computed based on a piecewise constant reconstruction of the free surface. The original VOF method has two main drawbacks. The first is that flotsam and jetsam can appear, which are small droplets disconnecting from the free surface [12,13]. The other drawback is the gain or loss of water due to rounding the VOF function when $F^s > 1$ or $F^s < 0$. By combining the VOF displacement with a local level set or height function, as described in the next paragraph, these drawbacks are highly reduced [16]. Another available variant with good mass conservation properties, is the piecewise linear reconstruction method PLIC of Youngs [19].

When the mass fluxes across the cell boundaries are known, the position of the free surface can be updated. Hereto a column or row of three cells centered around a S(urface) cell is considered, depending upon the orientation of the free surface (discussed in Section 3.2.1). In this column (or row) a local height function is defined, counting from the bottom of the column [15]. Fig. 5 (right) shows a situation with a horizontal liquid surface, where the column has been demarcated. Along the sides of the whole column of three cells the fluxes are added, and the new amount of liquid inside the column is determined. Herewith the local height function for the column is updated. The individual VOF values of the three cells are subsequently calculated from the height of the fluid in the column. Because of the CFL condition (the surface cannot move more than one grid cell per time step), the column cannot become under- or overfull. Thus, the method is strictly mass conserving and almost no flotsam and jetsam appear [16].

3.2.3. Curvature and boundary conditions

The calculation of the curvature of the free surface is another point that requires attention. As our applications fall in the range of unit Weber number, capillary physics plays a relevant role, and an accurate calculation of the pressure jump across the free surface, see Eq. (3), is highly desired. It is well known that careless calculation of the pressure jump can lead to spurious velocities [31–35]. These unphysical velocities are very visible when a steady-state configuration is to be achieved, but they will influence unsteady flow results as well. Accurate curvature calculation can be obtained when the position of the free surface is described by means of the local height function as just defined [15,33,34]. Hereto, in a $3\times3\times3$ cube around the surface cell concerned, locally a height function is formed by adding the F^s values column wise in the direction indicated by the surface orientation (see Fig. 5). Thus in a 3×3 array of columns the discrete height h is known. Next the curvature can be computed from

$$2\kappa = \frac{\partial}{\partial x}\left(\frac{\partial h/\partial x}{\sqrt{1+(\partial h/\partial x)^2+(\partial h/\partial y)^2}}\right) + \frac{\partial}{\partial y}\left(\frac{\partial h/\partial y}{\sqrt{1+(\partial h/\partial x)^2+(\partial h/\partial y)^2}}\right), \tag{19}$$

in case the surface orientation is about horizontal, and from similar expressions in other cases. Eq. (19) is discretized using the 3×3 array of columns: the first-order derivatives of h are discretized on the faces of the central column, yielding the final expression in the column's center with second-order accuracy.

It is remarked that in well resolved situations, where the surface on a three-cell scale remains fairly straight, a 3×3 array of columns (rows) mostly suffices. This is due to our decision criterion for the orientation of the free surface, which is based on the slope of the cell diagonal. For instance, consider the liquid surface in Fig. 6 which we decide to be 'vertical'. If it would have been decided 'horizontal', the decision in case the physical normal would be used, then obviously more rows would have been needed to give an accurate calculation of the curvature, e.g. a 5×3 array; [34] uses even a 7×3 array.

The obtained value for the curvature is substituted in the first condition in (3). The latter acts as a boundary condition for the pressure. In its discrete version it is written as a condition between the pressure in the corresponding S(urface) cell and a selected neighbouring F(luid) cell (based on the surface orientation). The condition

is applied at the liquid surface, where the pressure is taken as a linear interpolation between the pressure in the two cells just mentioned. This approach was already used in [9].

Usually, a S(urface) cell will be adjacent to one E(mpty) cell. The (S–E) velocity at the connecting face is found by invoking mass conservation in the S cell. When more E neighbours exist, individual derivatives are set equal to zero. The momentum equation between two S cells requires a velocity component between two neighbouring E cells; this component is computed from the tangential stress condition in (3), applied in the intersection point of two grid lines (a cell vertex). Again, here the original approach from [9] is followed. We have good experiences with this approach, except in the propagation of steep waves. In the latter application we compute the S–E velocities in a different way (extrapolated from the liquid interior); details can be found in [16].

3.3. Contact angle

Near the contact line, adhesive and cohesive forces are competing to determine the position of the free surface. Their effect usually is prescribed as a (static) contact angle θ: the angle between the normal of the free surface and the normal of the solid body at the contact line. The discretization of the contact angle is first explained in two dimensions, thereafter in three dimensions. A grid-refinement study gives an indication about the accuracy of the approach.

3.3.1. Two dimensions

In two dimensions, a typical configuration is sketched in the left of Fig. 7. Here the contact line is indicated by • and the normal of the solid body (pointing into the flow domain) is denoted by $\boldsymbol{n}_\mathrm{b}$ (see also [52], where only staircase approximations of the solid body are used for prescribing the contact angle). Now, for a given contact angle, two possible directions of the normal $\boldsymbol{n}_\mathrm{s}$ of the free surface remain. Based on the location of the liquid, a definite choice of the normal $\boldsymbol{n}_\mathrm{s}$ is made.

For example, in Fig. 7 the liquid is positioned in the lower part, whence the normal of the free surface points upward. With this normal vector, the local height function in S cells near the solid body can be computed as is demonstrated in Fig. 7 (right). Here the free surface is approximately horizontal, whence a horizontal height function is formed for the central S cell. Since the cell on the left of this cell is a B cell, no liquid height can be computed in the left-hand column of cells. Hence, in this column, the height is set to a value h_w, such that the line through h_w and h_c is perpendicular to the normal vector $\boldsymbol{n}_\mathrm{s}$. Note that in this example the boundary of the solid body is vertical and the free surface is approximately horizontal. In such a case, where the normal of the solid boundary and the normal of the free surface are classified as being perpendicular, it is sufficient to consider S–B cell faces for applying the contact angle in computing the local height function.

If the normal of the solid boundary and the normal of the free surface at the contact line have approximately the same direction, the occurrence of an S–B cell face is not sufficient for applying the contact angle. This is illustrated in Fig. 8, where a vertical height function for the central S cell is computed near a vertical wall. In this example the presence of an E cell above the S cell is necessary in order to discretise the contact

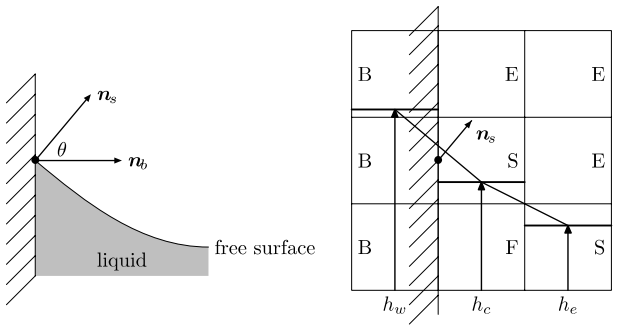

Fig. 7. Left: The contact angle θ is the angle between the normal $\boldsymbol{n}_\mathrm{b}$ of the solid boundary and the normal $\boldsymbol{n}_\mathrm{s}$ of the free surface at the contact line (which is indicated by •). Right: Horizontal local height function near a vertical wall.

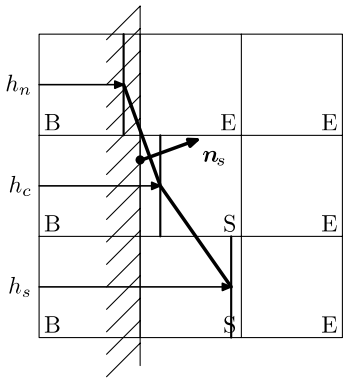

Fig. 8. Vertical local height function near a vertical wall.

angle. This is done by setting the height in the top row to a value h_n, such that the line connecting h_n and h_c is perpendicular to $\boldsymbol{n}_s$.

3.3.2. Three dimensions

Determining the normal $\boldsymbol{n}_s$ in three dimensions is more complicated than in two dimensions (see Fig. 9). Indeed, if the normal $\boldsymbol{n}_b$ at the solid boundary is given, then an infinite number of vectors make an angle θ with this normal vector. Two of these vectors are perpendicular to the tangent $\boldsymbol{t}_s$ of the contact line and therefore are candidates for $\boldsymbol{n}_s$. Based on the location of the liquid (like in two dimensions), a final decision for the normal of the free surface can be made. Thus, to be able to determine the direction of the normal of the free surface, both the normal of the solid boundary and the tangent to the contact line are needed. The computation of the former can be done analytically (if the shape of the flow domain is known analytically) or approximative using the volume and face apertures. The computation of the tangent $\boldsymbol{t}_s$ is based on the local height function. Hereto, first, an approximation of the direction of the contact line is determined by looking at the approximate Cartesian directions of the solid boundary and the free surface. For example, if the largest component of the normal of the solid boundary is the x-component and if the local height function for the S cell under consideration is formed in z-direction, then a first guess for $\boldsymbol{t}_s$ is given by $(0, 1, h'_y)$, where h'_y is a finite-difference approximation of $\partial h/\partial y$. Next, $\boldsymbol{t}_s$ is found by projecting this initial guess on the plane with normal $\boldsymbol{n}_b$. Finally, the normal $\boldsymbol{n}_s$ of the free surface at the contact line is given by a linear combination of $\boldsymbol{n}_b$ and $\boldsymbol{t}_s \times \boldsymbol{n}_b$, such that $\boldsymbol{n}_s$ makes an angle θ with $\boldsymbol{n}_b$ and points from the liquid into the air.

Similar to the technique described in two dimensions, the normal of the free surface at the contact line is used for constructing fictitious heights in B cells, which in turn can be used for computing the curvature of the free surface near the solid boundary.

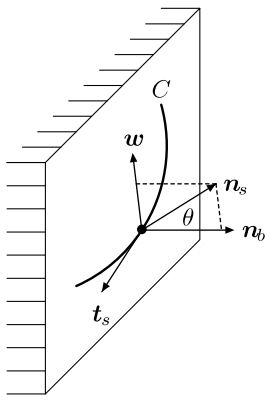

Fig. 9. In three dimensions, the normal $\boldsymbol{n}_s$ of the free surface makes an angle θ with the normal $\boldsymbol{n}_b$ of the solid boundary and lies in the plane spanned by $\boldsymbol{n}_b$ and $\boldsymbol{w} = \boldsymbol{t}_s \times \boldsymbol{n}_b$, where $\boldsymbol{t}_s$ is the tangent to the contact line C.

3.3.3. Grid refinement study

To validate the numerical treatment of wall adhesion and contact line issues in cut cells, a grid refinement study of capillary flow in a circular cavity (with unit radius) is shown next. Initially, the lower half of the flow domain is filled with liquid. The contact angle is set to $\theta = 30°$. Together with surface tension, this contact angle drives the flow.

In Fig. 10, snapshots (at time $t = 100$, when a steady state was reached) of the free surface are shown for grids consisting of 20×20, 40×40, and 80×80 cells. For these simulations, the Ohnesorge number $Oh \equiv \mu r_c / \sigma$, based on the cavity radius r_c, was equal to $Oh = 10^{-2}$. In this figure, bold lines show results from the simulation, while thin lines correspond to the theoretical steady-state solution. The grid consisting of 20×20 cells is clearly too coarse to accurately resolve the liquid dynamics; the somewhat finer grid with 40×40 cells gives adequate results. On the finest grid with 80×80 cells the difference between theory and simulation is hardly visible.

3.4. Discretization of the solid-body model

The discretization of Eqs. (9) and (10) can be given schematically as

$$m\dot{\boldsymbol{q}}^{n+1} + \dot{\boldsymbol{\omega}}^{n+1} \times m\bar{\boldsymbol{r}}^{n+1} = \mathscr{L}^n, \tag{20}$$

$$m\bar{\boldsymbol{r}}^{n+1} \times \dot{\boldsymbol{q}}^{n+1} + \boldsymbol{I}^{n+1}\dot{\boldsymbol{\omega}}^{n+1} = \mathscr{A}^n, \tag{21}$$

where the superscript again denotes the time level. The symbols $\mathscr{L}^n$ and $\mathscr{A}^n$ on the right-hand side contain $\boldsymbol{q}^n$, $\boldsymbol{\omega}^n$, as well as the fluid velocities $\boldsymbol{u}^{n+1}$ in the tank and the thruster forces $\boldsymbol{F}^{n+1}$ with their induced torques. The temporal derivatives are integrated from time level n to $n+1$ using a fourth-order Runge–Kutta method. Eqs. (20) and (21) lead to a linear system for six unknowns (three components of both $\dot{\boldsymbol{q}}$ and $\dot{\boldsymbol{\omega}}$), which is solved by means of Gaussian elimination during each Runge–Kutta step [15,39]. As indicated already in Section 2.3, the above formulation with the total (=solid + liquid) mass and inertia in the left-hand side is stable for any ratio between liquid mass and 'dry' spacecraft mass.

The philosophy of this coupling approach strives for a simultaneous treatment of both components as far as feasible: the 'solid part' of the liquid is combined with the Sloshsat body, only the liquid motion relative to the tank is left segregated. For a more detailed analysis of the stability behaviour of the algorithmic coupling between solid-body dynamics and liquid dynamics we refer to [4,15,39]. Similar algorithmic issues appear in many partitioned systems, like the simulation of floating objects [40] or in viscous–inviscid interaction [53].

The coupling in (20) + (21) has an explicit character. It is first-order accurate in time, consistent with the first-order accuracy of the free-surface displacement. In principle, an implicit time integration would also have been possible. Subiterations inside each time step then have to take care of the information exchange between solid body and liquid; an example can be found in [40].

3.5. Solution procedure

The simulation of a Sloshsat manoeuvre is started with a lasting period of (prescribed) rotation $\boldsymbol{\omega}$ around the stable axis of maximum MOI and zero linear velocity $\boldsymbol{q}$, without any thruster action. In this initial period,

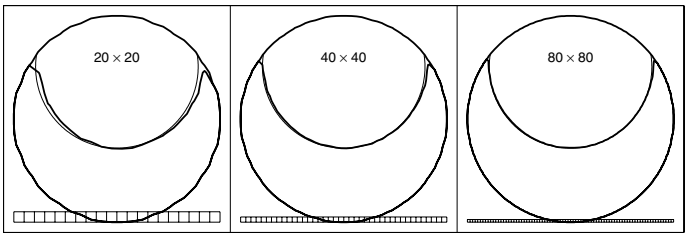

Fig. 10. Snapshots of the free surface in the steady-state solution ($\theta = 30°$) on grids of 20^2, 40^2, and 80^2 cells (a small part of the computational grid is shown in the bottom of the flow domain). Bold lines show results from the simulation, thin lines show the theoretical steady-state solution.

the water inside the tank can settle towards a stable configuration. Only the discretized conservation Eqs. (15) + (16) and the fluid displacement (18) are solved, as $\boldsymbol{\omega}$ and $\boldsymbol{q}$ are constant in this period. The calculated stable initial fluid configuration inside the liquid tank is shown in Fig. 11. Note that the center of gravity (i.e. the center of rotation) of the spacecraft (including liquid) is located far outside the geometric center of the tank (cf. Fig. 1). Also the main axes of inertia are not quite aligned with the Sloshsat coordinate axes (parallel to its sides). This explains the shape of the liquid surface.

The final state after the initial period is referred to as $t = 0$, and the manoeuvre is started. From this time, all discretized equations are solved in the sequential order (17) + (19), (16), (18), (20) + (21), after which the next time level is reached. At each time level, the influence of the thruster forces is incorporated when solving (20) + (21).

The discrete coupling approach has been verified on simple test cases, e.g. on a free-tumbling rectangular container without liquid, for which the dynamics can be calculated by analytical means [15,39].

4. Experiments and simulations

4.1. Experiments with Sloshsat

The experimental study of the interaction between liquid sloshing and spacecraft dynamics, by means of drop towers or parabolic flights, is limited because of the short duration of weightlessness that can be achieved: typically between 5 and 20 s. Therefore, experiments have been carried out in February 2005 with the satellite Sloshsat FLEVO in (geo-transfer) orbit around earth. During the experiments the spacecraft motion was measured with three orthogonal gyroscopes and with six high-quality accelerometers (Qflex 3000) that are positioned in three pairs at corners of the Sloshsat structure [5,49].

The Sloshsat tank shape has a cylindrical section of length equal to radius, capped by hemispherical ends, with a volume of 86.9 l (Fig. 1). The tank is partly filled with 33.5 kg of distilled water, which could freely move during the experiments. The dry mass of the spacecraft is 95 kg (which is less than three times the liquid mass). During 56 h over a period of 8 days, various experiments have been carried out, controlled by 12 thrusters that could be fired with a frequency of 30 Hz. The status of each thruster was recorded. The thruster forces that operate on the spacecraft can be estimated from the measured pressure inside the fuel tank (compressed nitrogen gas).

From the flight record about 26 h of data have been selected with Sloshsat at (near) equilibrium spin about its major axis of inertia. In this state the frozen spacecraft nutation frequency is about 1/3 of the spin rate. The data have been used to calibrate the accelerometer performances, a task that cannot be performed accurately on earth. The procedure yields a 1σ value of $O(5 \times 10^{-6}\ \mathrm{m/s^2})$ for the uncertainty of steady accelerometer data in a 30 mg range. In addition, data have been generated on the precession and nutation damping of Sloshsat with very little liquid flow. The precession is from torque by gas leaking from the Sloshsat high-pressure tubing, a mission anomaly. The liquid displacements allow to consider Sloshsat as a model of non-rigid planetary or cometary bodies. The nutation damping of these systems is a classical problem in astrodynamics [54], and the experiment data may serve to elucidate various aspects, e.g. the parity of the spin.

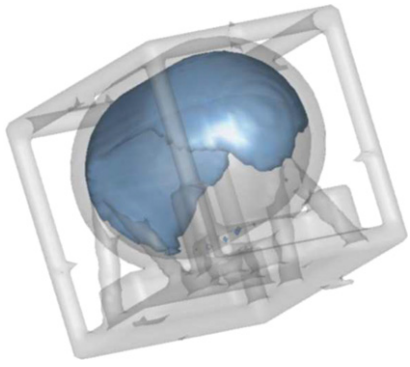

Fig. 11. An initial fluid configuration ($t = 0$) with Sloshsat in a stable configuration rotating around its axis of maximum MOI.

The calibrated accelerometers provide the experimental data for the planned and the supplemental investigations. These can be subdivided in four categories [5]: (i) spin-up and spin-down; (ii) liquid transfer manoeuvres; (iii) nutation avoidance manoeuvres, and (iv) flat spin. In this paper we will discuss the latter two types of experiments. Preliminary results for the other manoeuvres can be found in [55,56].

Nutation-avoidance manoeuvres (NAM) are meant to reposition the angular rotation vector of the spacecraft without inducing too much nutation. A practical example is an observational satellite that has to be pointed towards another direction. In such a case, heavy nutation in combination with a low level of damping is very undesirable. In theory, resulting nutation can be fully avoided by applying three thruster actions at suitable moments in time and with suitable strength [57]. As this theory does not account for sloshing liquid, the experiments are intended to study its disturbing effect.

The flat-spin experiments deal with large-scale fluid motion. In its starting position, Sloshsat is forced to rotate around the axis of intermediate MOI for some time, during which the fluid configuration can settle. Then, the thruster action is stopped, and a free tumble commences, during which the rotational direction of Sloshsat slowly moves towards the axis of maximum MOI. A large amount of nutation and fluid action is induced, hence such a manoeuvre is very challenging for the validation of the numerical model.

4.2. Comparison of measurements and simulations

In Fig. 12, a nutation avoidance manoeuvre is compared with a numerical simulation. The latter has been carried out on a relatively coarse grid, consisting of $30 \times 20 \times 20$ grid points. The (self-adjusting) time step is chosen such that the CFL number lies around 0.2, leading to a typical time step of 8×10^{-3} s. The simulation of 700 s real time lasted about 8 h on a 2.8 GHz PC.

The manoeuvre starts with an equilibrium fluid configuration corresponding with $\boldsymbol{\omega} = [0.003;\ -0.101;\ 0.007]^{\mathrm{T}}$. In the $\boldsymbol{\omega}_x$ component (top figure), the series of three thruster pulses can be distinguished. At $t = 0$ s, $t = 70$ s and $t = 140$ s, $\boldsymbol{\omega}_x$ decreases as a direct result of a short period of thruster action, followed by periods of free-tumble motion. The simulation is in reasonable agreement with the measurements of $\boldsymbol{\omega}_x$ and $\boldsymbol{\omega}_z$, with comparable nutation frequencies and amplitudes. The response to the thruster actions is correctly predicted. Note however that there is a slight drift in the $\boldsymbol{\omega}_y$ component. Calculations on a finer grid

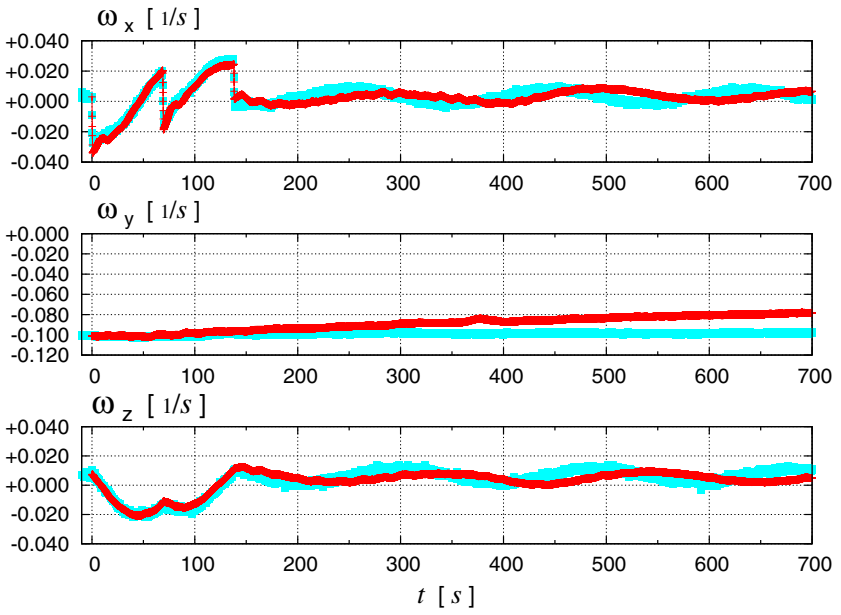

Fig. 12. The comparison of numerical simulation with measurements for the NAM experiment. The simulation is represented by the darker lines.

$45 \times 30 \times 30$ are very similar, and have therefore not been included in the graphs. Hence the differences between experiment and simulation cannot be attributed to lack of grid resolution. However, since the rotational speed is low and the NAM only induces small scale liquid motion, capillary forces (like stiction at the tank wall) can be important. Further improvement may be obtained by the use of a dynamic contact-angle model. In the simulations of drop tower experiments with liquid-filled cylinders, such models have already shown their usefulness [45]. This aspect is currently under study.

The flat-spin manoeuvre starts with a fluid configuration that is in equilibrium at $\boldsymbol{\omega} = [-0.005;\ 0.165;\ -0.011]^{\mathrm{T}}$. In the first 33 s, Sloshsat is approximately rotating around the axis of intermediate MOI. To give a global impression of the flat-spin manoeuvre, the Sloshsat orientation and water configuration during the simulation is depicted in Fig. 13. In the first subfigures, the water inside the tank is adapted to the rotation around the axis of intermediate MOI ($t < 33$ s). In the next subfigures, the fluid movement during the free tumble manoeuvre is shown. In the two final subfigures, the transition toward stable rotation around the axis of maximum MOI is almost completed ($t = 830$ s and $t = 831$ s). The orientation in these subfigures indicates a rotation period of $T \approx 12$ s, which is in agreement with $\omega_y \approx -0.55$ (Fig. 14).

The comparison between experiment and simulation is given in Fig. 14. A limited grid refinement study has been carried out on grids of size $30 \times 20 \times 20$ and $45 \times 30 \times 30$, respectively. The finer-grid calculation took about one day on a PC. At the end of the calculations the total liquid mass was conserved within 10^{-3}. On the finer grid, the obtained components of $\boldsymbol{\omega}$ from the simulation are in good agreement with those of the measurements. Both, the frequency and the amplitude of the spacecraft motion are correctly predicted. This experiment shows large-scale liquid motion, and hence numerical diffusion has a chance to become visible. Nevertheless, observe that on the finer grid the damping predicted by the simulations is quite comparable to that of the experiments. The coarser grid, however, shows too much (numerical) damping; it clearly does not suffice to catch the physics properly. Also, in earlier simulations of this manoeuvre using a first-order upwind discretization the damping was overpredicted [55,56].

The profile of ω_y shows modulation due to the different amplitudes of the ω_x and ω_z nutation. This difference comes from different moments of inertia and occurs at non-negligible nutation amplitude. The contribution of the liquid dynamics to this effect is to be investigated in detail.

5. Discussion

In this study, the influence of sloshing liquid on board spacecraft and satellites is investigated, as liquid management and its influence on the overall spacecraft dynamics is becoming increasingly important. Experiments have been carried out with the mini satellite Sloshsat FLEVO in an orbit around earth. These experiments were supported by a theoretical/computational model based on the Navier–Stokes equations for 3D

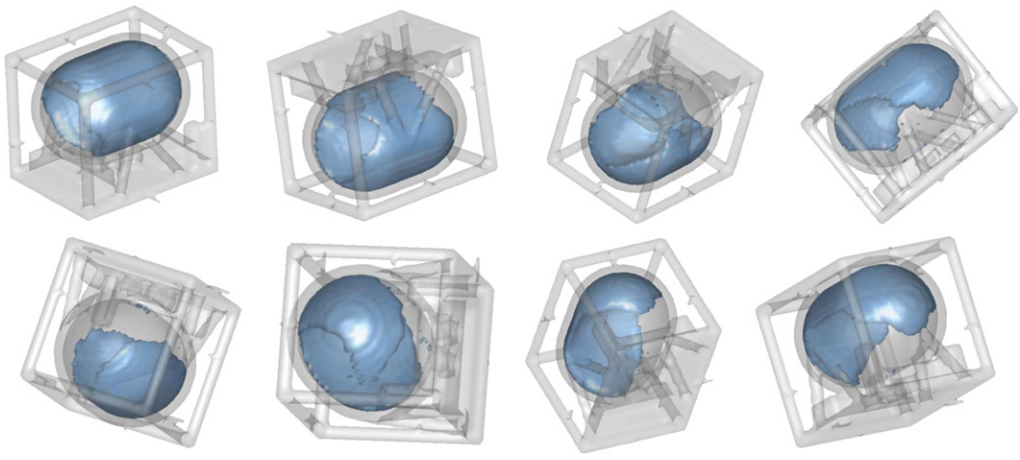

Fig. 13. Sloshsat orientation and water configuration during a flat-spin manoeuvre at $t = 14$, 18, 32, 37, 44, 64, 830 and 831 s (lexicographical order).

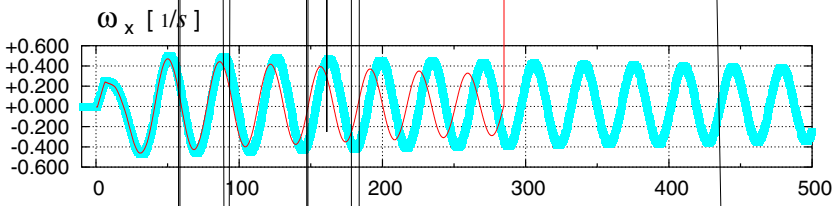

incompressible free-surface flow. This model includes capillary surface physics as well as coupled solid–liquid interaction dynamics.

A description has been presented of the numerical approach; several improvements over the original VOF method were indicated. The sometimes violent liquid motion requires the utmost of the numerics; the method was found highly robust. Further, a liquid–solid body coupling algorithm was presented that is stable for any mass ratio.

Measurements of the rotational velocity of Sloshsat have been compared with numerical simulations for two kinds of experiments, involving both small-scale and large-scale liquid motion. The obtained frequencies in angular velocities are quite comparable. This means that in the numerical model, the sloshing dynamics of the water inside the tank is reflected correctly by the satellite motion. The damping of the nutation amplitudes, observed in the simulations, is quite realistic. Comparison with earlier (first-order upwind) calculations shows that the use of a second-order upwind model significantly improves the numerical predictions (provided that the grid is chosen properly). The precise nature of the nutation damping merits closer investigation for its possible elucidation of planetary astrodynamics.

At low rotational rates and small-scale liquid motion, capillary effects are important. In the present numerical model, a constant contact angle is assumed. However, in reality the contact line probably (slightly) sticks to the tank wall, which means that there is less fluid motion in Sloshsat in comparison with the simulations. The use of a dynamic contact angle in the numerical model, as in [45], may yield a better agreement between simulation and experiments at low rotational velocities.

Acknowledgments

The research was funded by the National Institute for Space Research in the Netherlands (SRON), Projects MG-045 and MG-065.

Sloshsat FLEVO is a harmonized program between the European Space Agency (ESA) and the Netherlands Agency for Aerospace Programs (NIVR).

References

[1] Apollo 11 Lunar Surface Journal, The first lunar landing; mission time 102:38:20, <http://www.hq.nasa.gov/office/pao/History/alsj/a11/a11.landing.html>.
[2] NEAR Anomaly Review Board, The NEAR Rendezvous Burn Anomaly of December 1998, Johns Hopkins University, Applied Physics Laboratory, November 1999.
[3] J.J.M. Prins, Sloshsat FLEVO: Facility for liquid experimentation and verification in orbit, in: Proceedings of the 51st International Astronautical Congress, Rio de Janeiro, 2000, Paper IAF-00-J.2.05.
[4] J.P.B. Vreeburg, A.E.P. Veldman, Transient and sloshing motions in an unsupported container, in: R. Monti (Ed.), Physics of Fluids in Microgravity, Taylor and Francis Publishers, 2002, pp. 293–321.
[5] J.P.B. Vreeburg, Measured states of Sloshsat FLEVO, in: Proceedings of the 56th International Astronautical Congress, Fukuoka, 2005, Paper IAF-05-C1.2.09.
[6] R.W. Yeung, Numerical methods in free-surface flows, Ann. Rev. Fluid Mech. 12 (1982) 395–442.
[7] W. Tsai, D.K.P. Yue, Computation of nonlinear free-surface flows, Ann. Rev. Fluid Mech. 28 (1996) 249–278.
[8] R. Scardovelli, S. Zaleski, Direct numerical simulation of free-surface and interfacial flow, Ann. Rev. Fluid Mech. 31 (1999) 567–603.
[9] F.H. Harlow, J.E. Welch, Numerical calculation of time-dependent viscous incompressible flow of fluid with free surface, Phys. Fluids 8 (1965) 2182–2189.
[10] D. Juric, G. Tryggvason, A front tracking method for dendritic solidification, J. Comput. Phys. 123 (1996) 127–148.
[11] C.W. Hirt, B.D. Nichols, Volume of fluid (VOF) method for the dynamics of free boundaries, J. Comput. Phys. 39 (1981) 201–225.
[12] W.J. Rider, D.B. Kothe, Reconstructing volume tracking, J. Comput. Phys. 141 (1998) 112–152.
[13] D.J.E. Harvie, D.F. Fletcher, A new volume of fluid advection scheme: the stream scheme, J. Comput. Phys. 162 (2000) 1–32.
[14] M. Rudman, Volume-tracking methods for interfacial flow calculations, Int. J. Numer. Meth. Fluids 24 (1997) 671–691.
[15] J. Gerrits, Dynamics of liquid-filled spacecraft, Ph.D. thesis, University of Groningen, 2001. URL: dissertations.ub.rug.nl/faculties/science/2001/j.gerrits.
[16] K.M.T. Kleefsman, G. Fekken, A.E.P. Veldman, B. Iwanowski, B. Buchner, A volume-of-fluid based simulation methods for wave impact problems, J. Comput. Phys. 206 (2005) 363–393.
[17] B. Engquist, O. Runborg, A.-K. Tornberg, High-frequency wave propagation by the segment projection method, J. Comput. Phys. 178 (2002) 373–390.
[18] A.-K. Tornberg, B. Engquist, The segment projection method for interface tracking, Comm. Pure Appl. Math. 56 (2003) 47–79.
[19] D.L. Youngs, An interface tracking method for a 3d Eulerian hydrodynamics code, Technical Report AWRE/44/92/35, Atomic Weapons Research Establishment, 1987.
[20] T. Yabe, F. Xiao, T. Utsumi, The constrained interpolation profile method for multiphase analysis, J. Comput. Phys. 169 (2001) 556–593.
[21] S. Osher, J.A. Sethian, Fronts propagating with curvature dependent speed: algorithms based on Hamilton-Jacobi formulations, J. Comput. Phys. 79 (1988) 12–49.

[22] J.A. Sethian, Level Set Methods: Evolving Interfaces in Geometry, Fluid Mechanics, Computer Vision and Materials Science, Cambridge University Press, 1996.
[23] W.J. Rider, D.B. Kothe, Stretching and Tearing Interface Tracking Methods, AIAA Paper 95-1717, 1995.
[24] M. Sussman, E. Fatemi, An efficient interface preweerving level set redistancing algorithm and its application to interfacial incompressible fluid flow, SIAM J. Sci. Comp. 20 (1999) 1165–1191.
[25] D. Enright, R. Fedkiw, J. Ferziger, I. Mitchell, A hybrid particle level set method for improved interface capturing, J. Comput. Phys. 183 (2002) 83–116.
[26] M. Sussman, E.G. Puckett, A coupled level set and volume-of-fluid method for computing 3d and axisymmetric incompressible two-phase flows, J. Comput. Phys. 162 (2000) 301–337.
[27] S.P. van der Pijl, A. Segal, C. Vuik, P. Wesseling, A mass-conserving level-set method for modelling of multi-phase flows, Int. J. Numer. Meth. Fluids 47 (2005) 339–361.
[28] C.W. Hirt, A.A. Amsden, J.L. Cook, An arbitrary Lagrangian-Eulerian method for all flow speeds, J. Comput. Phys. 14 (1974) 227–253.
[29] J.J. Monaghan, Simulating free surface flows with SPH, J. Comput. Phys. 110 (1994) 399–406.
[30] Y. Andrillon, M. Doring, B. Alessandrini, P. Ferrant, Comparison between SPH and VOF free surface flow simulation, in: Proceedings of the 5th Numerical Towing Tank Symposium, 2002.
[31] S. Popinet, S. Zaleski, A front-tracking algorithm for accurate representation of surface tension, Int. J. Numer. Meth. Fluids 30 (1999) 775–793.
[32] D. Lorstadt, M.M. Francois, W. Shyy, L. Fuchs, Assessment of volume of fluid and immersed boundary methods for droplet computations, Int. J. Numer. Meth. Fluids 46 (2004) 109–125.
[33] S.J. Cummins, M.M. Francois, D.B. Kothe, Estimating curvature from volume fractions, Comput. Struct. 83 (2005) 425–434.
[34] M.M. Francois, S.J. Cummins, E.D. Dendy, D.B. Kothe, J.M. Sicilian, M.W. Williams, A balanced-force algorithm for continuous and sharp interfacial surface tension models within a volume tracking framework, J. Comput. Phys. 213 (2006) 141–173.
[35] D.J.E. Harvie, M.R. Davidson, M. Rudman, An analysis of parasitic current generation in volume of fluid simulations, Appl. Math. Model. 30 (2006) 1056–1066.
[36] J.U. Brackbill, D.B. Kothe, C. Zemach, A continuum method for modelling surface tension, J. Comput. Phys. 100 (1992) 335–354.
[37] A.E.P. Veldman, M.E.S. Vogels, Axisymmetric liquid sloshing under low gravity conditions, Acta Astronaut. 11 (1984) 641–649.
[38] J.P.B. Vreeburg, The Wet Satellite Model experiment, Technical Report, TP 94169, NLR, Amsterdam, 1994.
[39] J. Gerrits, A.E.P. Veldman, Dynamics of liquid-filled spacecraft, J. Eng. Math. 45 (2003) 21–38.
[40] G. Fekken, Numerical Simulation of Free-surface Flow with Moving Objects, PhD thesis, University of Groningen, The Netherlands, 2004. URL: dissertations.ub.rug.nl/faculties/science/2004/g.fekken.
[41] K.M.T. Kleefsman, Water Impact Loading on Offshore Structures – A Numerical Study, Ph.D. thesis, University of Groningen, The Netherlands, 2005. URL: dissertations.ub.rug.nl/faculties/science/2005/k.m.t.kleefsman.
[42] G.E. Loots, Fluid–structure Interaction in Hemodynamics, Ph.D. thesis, University of Groningen, The Netherlands, 2003. URL: dissertations.ub.rug.nl/faculties/science/2003/g.e.loots.
[43] G.E. Loots, B. Hillen, A.E.P. Veldman, The role of hemodynamics in the development of the outflow tract of the heart, J. Eng. Math. 45 (2003) 91–104.
[44] N.M. Maurits, G.E. Loots, A.E.P. Veldman, The influence of vessel wall elasticity and peripheral resistance on the flow wave form in the carotid artery: a CFD model compared to in-vivo ultrasound measurements, J. Biomech. 40 (2007) 427–436.
[45] S. van Mourik, A.E.P. Veldman, M.E. Dreyer, Simulation of capillary flow with a dynamic contact angle, Microgravity Sci. Techn. 17–3 (2005) 91–98.
[46] G. Yang, D.M. Causon, D.M. Ingram, Calculation of compressible flows about complex moving geometries using a Cartesian cut cell method, Int. J. Numer. Meth. Fluids 33 (2000) 1121–1151.
[47] M. Dröge, R. Verstappen, A new symmetry-preserving Cartesian-grid method for computing flow past arbitrarily shaped objects, Int. J. Numer. Meth. Fluids 47 (2005) 979–985.
[48] R.W.C.P. Verstappen, A.E.P. Veldman, Symmetry-preserving discretization of turbulent flow, J. Comput. Phys. 187 (2003) 343–368.
[49] A.E.P. Veldman, K.-W. Lam, Symmetry-preserving upwind discretization of convection on non-uniform grids, Appl. Num. Math. (accepted for publication).
[50] E.F.F. Botta, M.H.M. Ellenbroek, A modified SOR method for the Poisson equation in unsteady free-surface flow calculations, J. Comput. Phys. 60 (1985) 119–134.
[51] A.E.P. Veldman, M.E.S. Vogels, Axisymmetric liquid sloshing under low-g conditions: numerical simulation method – reference manual, Technical Report. TR 86057 U, National Aerospace Laboratory NLR, 1986.
[52] D.B. Kothe, R.C. Mjolsness, RIPPLE: a new model for incompressible flows with free surfaces, AIAA J. 30 (11) (1992) 2692–2700.
[53] A.E.P. Veldman, New, quasi-simultaneous method to calculate interacting boundary layers, AIAA J. 19 (1981) 79–85.
[54] M. Efroimsky, A. Lazarian, V. Sidorenko, Complex rotation with internal dissipation; application to cosmic-dust alignment and to wobbling comets and asteroids, in: S.G. Pandalai (Ed.), Recent Research Developments in Astrophysics, Research Signpost, India, 2002, pp. 59–116.
[55] R. Luppes, J.A. Helder, A.E.P. Veldman, Liquid sloshing in microgravity, in: Proceedings of the 56th International Astronautical Congress, Fukuoka, 2005, Paper IAF-05-A2.2.07.
[56] R. Luppes, J.A. Helder, A.E.P. Veldman, The numerical simulation of liquid sloshing in microgravity, in: P. Wesseling, E. Oñate, J. Periaux (Eds.), Proceedings of the ECCOMAS CFD 2006, Egmond aan Zee, 2006.
[57] E.B. Crellin, Nutation avoidance manoeuvre experiments on Sloshsat, unpublished document, ESA-Estec, August 2004.